

X-ray Emission Spectroscopy of Bulk Liquid Water in “No-man’s Land”

Jonas A. Sellberg^{1,2}, Trevor A. McQueen^{1,3}, Hartawan Laksmono⁴, Simon Schreck^{5,6}, Martin Beye⁵, Daniel P. DePonte^{7,8}, Brian O’Kennedy⁹, Dennis Nordlund¹⁰, Raymond G. Sierra⁴, Daniel Schlesinger², Takashi Tokushima¹¹, Iurii Zhovtobriukh², Sebastian Eckert⁵, Vegard H. Segtnan^{1,12}, Hirohito Ogasawara¹⁰, Katharina Kubicek^{13,14}, Simone Techert^{14,15}, Uwe Bergmann⁸, Georgi L. Dakovski⁸, William F. Schlotter⁸, Yoshihisa Harada^{16,17}, Michael J. Bogan⁴, Philippe Wernet⁵, Alexander Föhlisch^{5,6}, Lars G. M. Pettersson², and Anders Nilsson^{1,2,10}

¹*SUNCAT Center for Interface Science & Catalysis, SLAC National Accelerator Laboratory, 2575 Sand Hill Road, Menlo Park, CA 94025, USA;*

²*Department of Physics, AlbaNova University Center, Stockholm University, S-106 91 Stockholm, Sweden;*

³*Department of Chemistry, Stanford University, Stanford, CA 94305, USA;*

⁴*PULSE Institute, SLAC National Accelerator Laboratory, 2575 Sand Hill Road, Menlo Park, CA 94025, USA;*

⁵*Institute for Methods and Instrumentation for Synchrotron Radiation Research, Helmholtz-Zentrum Berlin für Materialien und Energie GmbH, Albert-Einstein-Straße 15, 12489 Berlin, Germany;*

⁶*Institut für Physik und Astronomie, Universität Potsdam, Karl-Liebknecht-Straße 24–25, 14476 Potsdam, Germany;*

⁷*Center for Free-Electron Laser Science, DESY, Notkestraße 85, 22607 Hamburg, Germany;*

⁸*Linac Coherent Light Source, SLAC National Accelerator Laboratory, 2575 Sand Hill Road, Menlo Park, CA 94025, USA;*

⁹*MAX-lab, PO Box 118, 221 00 Lund, Sweden;*

¹⁰*Stanford Synchrotron Radiation Lightsource, SLAC National Accelerator Laboratory, P.O. Box 20450, Stanford, CA 94309, USA;*

¹¹*RIKEN SPring-8 Center, 1-1-1 Kouto, Sayo-cho, Hyogo 679-5148, Japan;*

¹²*Nofima AS, N-1430 Ås, Norway;*

¹³*Photon Science, DESY, Notkestraße 85, 22607 Hamburg, Germany;*

¹⁴*IFG Structural Dynamics of (Bio)chemical Systems, Max Planck Institute for Biophysical Chemistry, Am Faßberg 11, 37070 Göttingen, Germany;*

¹⁵*Advanced Study Group of the MPG, CFEL, Notkestraße 85, 22853 Hamburg, Germany;*

¹⁶*Institute for Solid State Physics (ISSP), University of Tokyo, Kashiwanoha, Kashiwa, Chiba 277-8581, Japan;*

¹⁷*Synchrotron Radiation Research Organization, University of Tokyo, Sayo-cho, Sayo, Hyogo 679-5198, Japan*

The structure of bulk liquid water was recently probed by x-ray scattering below the temperature limit of homogeneous nucleation (T_H) of ~ 232 K [J. A. Sellberg *et al.*, *Nature* **510**, 381-384 (2014)]. Here we utilize a similar approach to study the structure of bulk liquid water below T_H using oxygen K-edge x-ray emission spectroscopy (XES). Based on previous XES experiments [T. Tokushima *et al.*, *Chemical Physics Letters* **460**, 387-400 (2008)] at higher temperatures, we expected the ratio of the $1b_1'$ and $1b_1''$ peaks associated with the lone-pair orbital in water to change strongly upon deep supercooling as the coordination of the hydrogen (H-) bonds becomes tetrahedral. In contrast, we observed only minor changes in the lone-pair spectral region, challenging an interpretation in terms of two interconverting species. A number of alternative hypotheses to explain the results are put forward and discussed. Although the spectra can be explained by various contributions from these hypotheses, we here emphasize the interpretation that the line shape of each component changes dramatically when approaching lower temperatures, where, in particular, the peak assigned to the proposed disordered component would become more symmetrical as vibrational interference becomes more important.

I. INTRODUCTION

Water has been studied intensively for hundreds of years but is still far from fully understood. Knowledge about the H-bond network in water is essential for understanding its numerous unusual chemical and physical properties. For example, water can remain in the liquid state far below its melting temperature (supercooled water) where its thermodynamic response functions, such as coefficient of thermal expansion (α_P), isothermal compressibility (κ_T), isobaric heat capacity (C_P) and correlation length (ξ) appear to diverge at a difficult to reach temperature of 228 K^{1-3} . Water crystallization occurs very rapidly below the homogeneous nucleation temperature (T_H) of $\sim 232 \text{ K}^4$, which has prevented measurements of the liquid phase and led to a “no-man’s land” devoid of experimental results. The anomalous behavior of water becomes important already at ambient conditions giving a maximum density at 277 K , and a minimum in C_P and κ_T at 308 K and 319 K , respectively.

The apparent divergence of C_P and κ_T upon supercooling has led to several proposed scenarios involving fluctuations between local high-density liquid (HDL) and low-density liquid (LDL) configurations. These fluctuations could, upon deeper supercooling, lead either to a liquid-liquid transition (LLT) with a liquid-liquid critical point (LLCP) at positive pressure⁵ or a continuous transformation without discontinuity, called the singularity-free (SF) model⁶. In the critical point-free model (CPF) the LLCP would instead occur at negative pressure⁷ (outside the physically relevant part of the phase diagram), but there is also a recent suggestion that only a liquid-solid transition exists⁸, which is currently under debate⁹⁻¹⁴. Alternatively, a thermodynamic stability limit (SL) of the liquid state has been suggested¹⁵ and that ice crystallization occurs on a timescale faster than liquid equilibration in “no-man’s land”¹⁶. These scenarios do not agree, and to date convincing

experimental data have been lacking. Recently a new technique has been demonstrated where it is possible to enter “no-man’s land” through fast evaporative cooling of micron-sized water droplets and ultrafast probing using x-ray scattering from an x-ray laser¹⁷. It was shown that water could be probed in a metastable liquid phase down to 227 K and that a continuous increase of structures with local tetrahedral coordination became more enhanced upon deep supercooling, which indicates an accelerated transition toward LDL.

There are several spectroscopic techniques such as vibrational spectroscopy and core-level spectroscopy that are sensitive to the hydrogen-bonding (H-bonding) environment¹⁸. In particular recent x-ray emission (XE) spectra show a split of the lone-pair ($1b_1$) peak in water^{19,20} that has been interpreted as arising from structures with distorted H-bonds ($1b_1''$) and from tetrahedrally H-bonded structures ($1b_1'$)^{18,20-27}. As the liquid temperature is raised, intensity is transferred from the low-energy $1b_1'$ peak to the high-energy $1b_1''$ peak, but no broadening or additional features are observed^{20,28}. Also, selective excitations show a clear correlation between the two $1b_1$ peaks and the various resonances in the x-ray absorption spectrum of water consistent with the hypothesis of two structural motifs^{20,28}. An interpretation has been proposed in terms of these local structures being related to fluctuations in the liquid giving rise to local regions of HDL (distorted) and LDL (tetrahedral) character^{18,24,28,29}.

However, the strong isotope effect in the spectra has led to other suggestions of the origin of the two $1b_1$ peaks^{19,20}. The first alternative interpretation suggests that the two peaks are due to intermediate or final states of ultrafast dissociation during the core-hole lifetime^{19,30}. The peak at low emission energy was proposed to come from OH species generated from water through core-hole-induced dissociation while the other was proposed to be due to intact water^{19,30}. The second alternative interpretation, based on theoretical simulations, proposed that the peak at high energy is of lone-pair $1b_1$ symmetry, whereas the peak at low emission energy is of $3a_1$ symmetry and originating from the strong dynamical response toward dissociation found in the simulations^{31,32}. Excitation-selective, polarization-dependent measurements indicated first that there could be a difference between the two peaks in terms of symmetry³³, but later more data and better statistics demonstrated that the two lone-pair peaks are both of b_1 symmetry ruling out that the $1b_1'$ peak would be of a_1 symmetry²⁷. Furthermore, theoretical calculations of the XE spectrum of a model water dimer including vibrational-lifetime interference in a full Kramers-Heisenberg treatment show only the appearance of an asymmetrical line shape and not two distinct peaks^{34,35}. The asymmetry of the b_1 peak of the lighter isotope is much larger which could explain the isotope effect.

Based on the interpretation in terms of two structural motifs, we would expect a rapid rise in intensity for the $1b_1'$ peak if the liquid is cooled down to temperatures within “no-man’s land”. Here we show that this is not the case. We will review several possible explanations for this result. Although no definite conclusion can be drawn it is essential that these data are made available, since it is the first XES study of liquid water venturing into “no-man’s land” and since it led to results in seeming contradiction to expectation.

II. METHODS

A. Experimental setup at SXR, LCLS. Non-resonant O K-edge XES was performed at the Soft X-ray Materials Science (SXR) instrument³⁶ at the Linac Coherent Light Source (LCLS) using a nominal photon energy of 550 eV (well above the O K-edge absorption resonance) and a nominal pulse duration of 100 fs. These pulses, delivered at 120 Hz and containing between 6×10^{11} and 12×10^{11} photons/pulse (accounting for 10 % beamline transmission from gas detectors to the sample³⁷), were focused to a focal spot size of $75 \times 520 \mu\text{m}^2$ (horizontal \times vertical) at the interaction point, corresponding to a peak fluence of 0.27 J/cm^2 , which is comparable to the threshold of $\sim 0.2 \text{ J/cm}^2$ where a non-linear fluence dependence of the XE yield starts to occur due to valence-hole reabsorption³⁷. Liquid D₂O (Fischer Scientific #AC166311000, 99.95 %; and Sigma-Aldrich #151882, 99.9 atom %) was delivered to the interaction region using the Liquid Jet End Station (LJE), which consists of a liquid microjet in a differentially pumped high vacuum (2×10^{-3} mbar at the jet, 4×10^{-7} mbar at the detector) and a Graze spectrometer XES 350³⁸ mounted at 90° with respect to the incident x-ray beam, as described in detail elsewhere³⁹. The liquid microjet was produced by a gas-dynamic virtual nozzle⁴⁰ (GDVN) operated at 800 psi liquid pressure and 330 psi He gas pressure. The microjet underwent Rayleigh breakup⁴¹ after a few hundred microns, driven by a piezoelectric actuator at 900 kHz (sine wave with 50 V amplitude), producing a single-file train of uniform droplets with a diameter of 5 μm , droplet spacing of 16 μm , and droplet speed of 14 m/s. The droplet diameter D_{drop} , droplet spacing $l_{\text{drop-drop}}$, and droplet speed v were estimated by mass conservation for a single-file droplet train of uniform diameter, namely $v = Q/A_{\text{jet}}$, $l_{\text{drop-drop}} = v/f$, and $D_{\text{drop}} = (3Q/4\pi f)^{1/3}$, where f is the droplet frequency determined by the piezoelectric actuator, Q is the *in situ* measured volume flow rate of 3.6 $\mu\text{l/min}$, and A_{jet} is the cross-sectional area of the initial liquid jet, determined to be $4.2 \mu\text{m}^2$ at given flow rate using a scanning electron microscope. Due to the large vertical focal spot size compared to the droplet spacing, up to 34 droplets were probed simultaneously for each shot; each spectrum was averaged over up to 2×10^6 shots, resulting in at least 90 000 detected photons. The distance between the dispenser nozzle and the interaction point, which determines the temperature of water droplets, is controlled by a 3-axis motorized sample stage. The temperature was estimated using Knudsen theory of evaporation⁴²⁻⁴⁴, which is mainly dependent on the droplet diameter, droplet speed, and the extrapolation of thermodynamic parameters into “no-man’s land” (see supplementary information in Sellberg *et al.*¹⁷ for details). During cooling, the droplets lose up to about 13 % of their mass through evaporation; the temperature within individual droplets can be considered homogeneous with differences less than 0.2 K between core and surface after 1 ms of travel time. The cooling is expected to be delayed due to the surrounding He gas, resulting in a temperature close to the room temperature $T_0 \approx 293 \text{ K}$ for measurements up to 0.8 mm away from the nozzle. Hence, the total uncertainty in temperature is estimated to be 290_{-7}^{+3} K , 226_{-1}^{+2} K , and 222_{-3}^{+5} K at $0.6 \pm 0.4 \text{ mm}$, $24.4 \pm 0.4 \text{ mm}$, and $45.5 \pm 0.3 \text{ mm}$ away from the nozzle, respectively, where XE spectra were recorded. Surface tension generates a pressure on droplets which here, however, is negligible, since it corresponds to a pressure increase of $\sim 0.6 \text{ bar}$.

B. Data analysis at LCLS. Emission spectra were recorded at 550 eV incident photon energy on a CsI coated multi-channel plate (MCP) stack combined with a phosphor screen monitored by a charge-coupled device camera (Opal 1000, Adimec), read out by the LCLS data acquisition system. Data were processed by single-photon identification. The photon positions were characterized by the center of mass of the fluorescent signal and translated to energy scale by projection onto the x -axis of the detector after a quadratic curvature correction. The absolute energy was calibrated by shifting the $1b_1''$ and $1b_2$ peaks of the spectrum recorded at ~ 290 K to their previously determined positions²⁸ of 526.78 eV and 521.10 eV, respectively; the corresponding XE spectra had an energy binning of ~ 75 meV. All XE spectra were background subtracted with an 8th order polynomial and area normalized between 500 eV and 550 eV.

C. Experimental setup at BL17SU and BL07LSU, SPring-8. Temperature-dependent O K-edge XES was performed at BL17SU at SPring-8, Japan, details of which have been described elsewhere⁴⁵. The fluence dependence experiment was performed at BL07LSU at SPring-8, Japan. The liquid flow-through cell system used was basically the same as used at BL17SU²⁶, whereas the XE spectrometer has higher total energy resolution⁴⁶ ($E/\Delta E \sim 5000$) than the one at BL17SU due to its long optical path length as well as coma-free mode operation⁴⁷. The incident photon flux was varied by tuning the front end slit placed at the upper stream of the monochromator, which only changes the fluence but affects neither the energy resolution nor the spot size at the sample position. Using this setup, we can thus precisely study the fluence dependence of the O K-edge XE spectra of liquid H₂O. In contrast to the free-electron laser measurements described in Sec. II A, the synchrotron measurements at SPring-8 were performed with picosecond x-ray pulses (~ 50 ps) at much higher repetition rates⁴⁸ (~ 500 MHz), resulting in that more than one pulse probe the same volume and that much lower fluences are obtained than at the free-electron laser. Hence, the fluence measurements are very different from the previous study by Schreck *et al.*³⁷ using LCLS to probe valence-hole reabsorption.

D. Simulated XE spectra. The calculations were performed using density functional theory for cluster models containing 32 molecules. Ten structures were extracted as a sampling of the vdW-DF2 *ab initio* molecular dynamics NVE simulation of 64 water molecules performed by Møgelhøj *et al.*⁴⁹. The central water was computed as either intact or as one of the fragments (O, O⁺, OH, OH⁺). Spectra were calculated using the ground state orbitals⁵⁰ and shifted such that the $1b_1''$ peak computed for H₂O coincides with the experimental position; spectra for the fragments were shifted by the same amount assuming that the neglected relaxation effects are similar in all cases. Emission energies and transition probabilities were computed with orbital-based density functional theory with the deMon2k code⁵¹ and the revised Perdew, Burke, and Ernzerhof⁵² (revPBE) gradient-corrected functional. The IGLO-III basis set of Kutzelnigg *et al.*⁵³ was used to represent the oxygen of the core-excited molecule. In the other oxygens the $1s$ core electrons were replaced by an effective core potential⁵⁴ and the remaining electrons were described using $4s4p$ basis functions contracted to $2s2p$. All hydrogens were described using $5s2p$ functions contracted to $2s2p$.

III. RESULTS

Fig. 1 shows XE spectra measured at LCLS at non-resonant conditions (550 eV) on the water droplets at three different temperatures corresponding to ~ 290 K, 226_{-1}^{+2} K and 222_{-3}^{+5} K. We notice quite small changes in the relative peak heights of the low-energy $1b_1'$ and high-energy $1b_1''$ peaks, but the $1b_1''$ peak width narrows with decreasing temperature, resulting in a shift of the center of mass of the peak from 526.74 eV at ~ 290 K to 526.66 eV and 526.63 eV at 226_{-1}^{+2} K and 222_{-3}^{+5} K, respectively. Because the XE spectrum of crystalline ice⁵⁵ only shows a prominent $1b_1'$ peak with the high-energy $1b_1''$ peak reduced to a weak shoulder, we may exclude that a significant volume fraction of the illuminated droplets would have crystallized prior to detection upon supercooling the liquid. We note that the two peaks are less well-resolved in comparison to previous measurements, which can be attributed to different energy resolution. Fig. 2 shows that the LCLS data at ~ 290 K can be fitted with relative intensities between the two components similar to high-resolution data measured at BL17SU at SPring-8 at 300 K if one accounts for the different instrumental resolutions and an additional background in the LCLS data from diffuse scattering from the grating due to imperfections, most likely originating from contamination.

Based on that the spectra at ~ 290 K measured at LCLS and at 300 K measured at SPring-8 can be fitted with similar populations of species related to distorted and tetrahedral H-bonds, we can decompose the spectra into relative populations as a function of temperature using the LCLS data at lower temperatures while using the SPring-8 data^{20,28} at higher temperatures. For this decomposition we assume that the line shapes of the two components are independent of temperature. Fig. 3 shows the temperature dependence of the relative populations of the $1b_1'$ and $1b_1''$ components as obtained under this assumption. It is clear that the fraction of distorted H-bonds is decreasing and the fraction of tetrahedral H-bonds is increasing with decreasing temperature, consistent with previous findings^{20,28}. Furthermore, we also observe the change in the high-energy $1b_1''$ peak position toward lower emission energy (Fig. 1) to be consistent with the previous studies. However, there is a major discrepancy as to what we would expect in terms of intensity of the low-energy $1b_1'$ peak in “no-man’s land” where the liquid is expected to become LDL-like with tetrahedral H-bonds. Analysis of inherent structures from the TIP4P/2005 force field shows that at 230 K the LDL and HDL populations should reach a 1:1 ratio and at temperatures below 230 K the LDL population should dominate^{24,56}. This is supported by experiments in “no-man’s land” where it was found that the tetrahedrality in terms of the peak height of the 2nd shell in the O-O pair correlation function becomes exceptionally strong and mimics low-density amorphous (LDA) ice¹⁷. The experimental temperature-dependent trend shows an even stronger increase in tetrahedrality than what is obtained from the TIP4P/2005 simulations¹⁷. We would therefore expect that at 226 K a crossing between the $1b_1'$ and $1b_1''$ populations would have occurred with the low-energy $1b_1'$ peak (interpreted as corresponding to local regions of LDL) becoming dominant. Clearly, this is not observed in Fig. 3.

IV. DISCUSSION

The lack of strong temperature dependence in the peak heights of the $1b_1'$ and $1b_1''$ peaks opens questions regarding our detailed understanding of the XE process and its connection to the structure of the liquid. The XE energy corresponds to the difference in binding energy of the $1b_1$ and $O1s$ orbitals as could also be measured through photoelectron spectroscopy. We note first that the valence photoelectron spectrum of water only shows one peak in the lone-pair region and that this is too sharp to support two contributions at the separation observed in XES⁵⁷⁻⁵⁹. Core-level photoelectron spectroscopy of liquid water shows only one $O1s$ peak as well, but in this case the $O1s$ peak is broad enough to support two unresolved features within the separation between the two $1b_1$ peaks in XES⁶⁰. Here we will discuss various hypotheses that can explain the current data. We are thereby revisiting an old discussion²⁵, but with a focus on that the temperature dependence is somewhat unexpected.

First, could the dissociative mechanism better explain the appearance of the two peaks^{19,31,32}? This has recently been extensively reviewed²⁵ and excluded based both on high-level theoretical simulations of a model water dimer^{34,35} and polarization-dependent measurements²⁷. It was shown that, although the potential energy surface in the core-excited state has its minimum at the accepting oxygen, the proton becomes delocalized between the two water molecules and the resulting O-H stretch has to be described as a superposition of several excited vibrational states, giving rise to important interference effects when the appropriate Kramers-Heisenberg formalism is applied. Indeed, the computed XE spectrum of the water dimer does not exhibit two distinct peaks but rather an asymmetrical $1b_1$ line shape that can also explain the isotope effect^{25,34,35}. Furthermore, the difference in binding energy between $1b_1$ and $O1s$ in photoelectron spectroscopy is nearly identical for OH and water²⁶, thus not giving an extra feature in the $1b_1$ region and, in addition, we would expect to see a distinct feature at 523 eV characteristic of a well-defined OH species²⁵. A dissociative mechanism involving OH and giving a sharp spectral feature in the lone-pair spectrum, but not at 523 eV, thus cannot account for the dependence of the two peaks on temperature²⁸, polarization²⁷ and excitation energy^{20,25,27,28}.

A second possibility is that the two peaks observed in XES reflect an additional and different bimodal distribution than that given by distorted and tetrahedral H-bonds which then could have temperature dependence different from that expected for HDL and LDL from molecular dynamics simulations. This seems highly unlikely, however, and there is currently no suggestion from simulations or theoretical considerations of any additional division of structures into classes with the observed weak temperature dependence and which would give rise to the two peaks in XES but be distinct from the suggested species.

A third explanation could be that the split is due to a ground state electronic structure effect in the liquid which depends on the local environment where the $1b_1$ peak is split due to band structure effects as for the $3a_1$ in ice^{57,61}. The argument against such an interpretation is that the valence photoelectron spectrum of liquid water should then also show two such peaks in the lone-pair region^{57,61}. In particular, measurements at relatively low photon energy, where the photoionization

cross section is dominated by the $O2p$ contribution^{57,61}, should give spectra similar to XES which is also completely derived from the $O2p$ character through the dipole selection rule for O K-edge emission. This however is not observed.

A 4th hypothesis is that there could be radical species building up in the liquid, not from ultrafast dissociation, but from the Auger decay cascade⁶². These could include various fragmented water species, such as the OH radical, that could contribute to the $1b_1'$ peak. This is contradicted by theoretical calculations of the $1b_1$ to $O1s$ emission energy for OH, OH^+ , O and O^+ as fragments, which all lead to a contribution at the $1b_1''$ position of intact water or at higher energy (Fig. 4). The theoretical results are further supported by experiments shown in Fig. 5 where high-resolution spectra of room temperature water, in this case H_2O , were measured at different incident fluence at BL07LSU at SPring-8 to see if the $1b_1'$ could be related to some fragmentation processes; since more fragments would be expected at higher fluence the $1b_1'$ peak would be expected to be enhanced at higher fluence. In agreement with the calculations no specific additional intensity grows in the $1b_1'$ region with increasing fluence, indicating that this feature is not related to OH, OH^+ , O or O^+ fragments. However, there is a small and almost negligible conversion of some $1b_1'$ to $1b_1''$ intensity with increasing fluence that will be discussed below. Although the currently tested radical species are the most probable⁶² we cannot definitely rule out that there could exist other species not tested here that could give rise to spectral intensity at lower energies. We note that non-linear effects in terms of reabsorption can affect the spectra but only at significantly higher fluence than the peak fluence in the present work³⁷.

A 5th hypothesis is that there is beam-induced transformation, not in terms of dissociation but in terms of local structural environment. This has been suggested in a recent study of the x-ray absorption spectra of cubic and hexagonal ice in order to explain the variation of the pre-edge intensity in various samples and using different measurement techniques⁶³. It was proposed that even if the ice is prepared as a pure hexagonal ice phase, the interaction with the beam may transform portions of the ice from hexagonal to high-density amorphous (HDA) ice. It is known that the enthalpy difference between ice I_h and HDA ice is 0.58 ± 0.1 kcal/mol⁶⁴ at 1 atm while the absorption of a photon at 550 eV corresponds to 12680 kcal/mol, which is 4 orders of magnitude higher and thus more than sufficient to convert ice I_h into HDA ice if the energy is not efficiently transferred away from the excited molecule. We postulate that the absorbed energy will dissipate slowly through the solid in the case of ice, creating many sites where significant energy is dumped and causing a local pressure rise that converts a fraction of the volume into HDA ice. Since the low temperature hinders thermal motions, these molecules are kinetically hindered to convert back to low-density hexagonal ice.

In the liquid state, at ambient temperatures, the large thermal motion and ultrafast dynamics of breaking and forming H-bonds on a picosecond timescale⁶⁵ allow for a beam-induced structural defect to convert back nearly instantaneously and no beam-induced structural transformation will be seen. This can account for the almost negligible intensity redistribution at room temperature in connection to Fig. 5. However, as water is supercooled below T_H the relaxation time in the liquid will

increase significantly. It has been shown that the structural relaxation time at 220 K in simulations of liquid water using the TIP4P/2005 water model is ~ 10 ns⁶⁶. Under a certain flux that transforms the liquid and if the rate to transform back to the structures at equilibrium is slow due to long relaxation time there could build up a steady-state concentration in deeply supercooled water of distorted H-bonds through this deposited energy resulting in converting some of the $1b_1'$ to $1b_1''$ intensity. The effect would become more prominent the colder the liquid becomes through the increasing relaxation time. The challenge to this hypothesis is that the x-ray pulse from LCLS is only around 100 fs in duration and the question is if the liquid would have time to undergo any transformation within this time period. A vibrational period in the H-bond translational mode is around 200 fs^{67,68}, which is relatively slow in comparison to the pulse length. However, regarding the deposited energy as equivalent to a local heating of the liquid it is most likely the librational mode that will mediate a structural transformation, where the water molecule will rotate out to avoid directional H-bonds. When comparing HDA ice to LDA ice, it is mostly bending of H-bonds that occurs⁶⁹ and we anticipate similar changes in a conversion of tetrahedrally H-bonded structures to local structures with distorted H-bonds at low temperatures. The vibrational period of the librational mode is of the order of 50 fs and a fractional period of motion could occur on a few femtoseconds to tens of femtoseconds timescale. This could result in a high rate of structural transformation, since the intensity during the LCLS pulse is very high, allowing for many excited molecular centers. Note however, that even if such a conversion would occur in soft x-ray experiments using free-electron lasers, we do not expect this effect to be significant for the recently performed hard x-ray scattering experiment at LCLS¹⁷, since at 9.4 keV the absorption cross section is lowered by several orders of magnitude in comparison to just above the O K edge.

Finally, a 6th hypothesis is that a modified fitting scheme of the two components is required, where also the line shape depends on temperature. It is most likely that the local structures with distorted and tetrahedral H-bonds will undergo changes with temperature. This is seen through the high emission energy $1b_1''$ peak position changing with temperature^{20,28} similarly to what is also seen in the XAS temperature-dependent spectra^{28,70}. We could view the two structural motifs as two different ensembles of molecules so that the line shape of the two peaks could depend on the temperature and not only on the distribution of species within each subensemble. This could occur through the local environment affecting the vibrational lifetime interference causing a change in the degree of asymmetry in the line shape. Let us first demonstrate that this is possible by simply changing the line width of the $1b_1'$ and $1b_1''$ components in the 222 K spectrum as shown in Fig. 6. Since the spectral resolution in the LCLS spectra is lower than in the SPring-8 spectra, the minimum between the $1b_1'$ and $1b_1''$ peaks is not well resolved in the LCLS spectra. This, together with the lower signal-to-noise ratio, allows for a wide range of spectral component widths to be consistent with the data and opens up a possibility that these can indeed undergo a large change with temperature, in particular in the deeply supercooled region; note that the higher resolution and better statistics of the SPring-8 spectra puts stricter limits on this range. Fig. 6 demonstrates that nearly any ratio between the two components can be achieved and if the line width would be allowed to change with temperature we can obtain an equal ratio between the two components as we enter into “no-man’s

land". Fig. 7 shows how we can fit the spectra with temperature-dependent line shapes to reconcile the expected nearly equal ratio between structures with tetrahedral and distorted H-bonds in terms of the area of the $1b_1'$ and $1b_1''$ components at 222 K. The basis for such a variation is a proposed picture of how the structure of the liquid evolves with decreasing temperature¹⁸.

In this picture, water behaves as a simple liquid at temperatures close to the boiling point, where most interactions are isotropic and dominated by non-directional van der Waals interactions⁷¹. As the liquid cools down, the water molecules start to stick to each other through directional H-bonds. This will appear through two classes of configurations^{18,24,28,29}, tetrahedral structures with four strong H-bonds (LDL-like regions) and asymmetric structures with distorted H-bonds (HDL-like regions), with fluctuations between them on some timescale. The first class of structures is enthalpically favored due to efficient H-bonding. Since cooperativity effects make the bonds stronger if water is H-bonded to other waters that are also in tetrahedral structures, fluctuations into tetrahedral structures expand into small local regions that become LDL-like in terms of their structure. The second class of structures is characterized by asymmetric local coordination with fewer, but paired, donor-acceptor H-bonds. With less directional H-bonds there is more flexibility for librational and translational motions and thereby higher entropy. The OH groups that are involved in either a strong or weak H-bond can switch on a very fast timescale. In this class of structures, isotropic molecular van der Waals interactions are important causing interstitial molecules to come in from a collapsed 2nd shell also generating distortions around the 1st shell. Since in this case there are more water molecules in the first coordination shell (defined out to 3.5 Å rather than to the minimum in $r^2g_{OO}(r)$ at 3.30 Å⁷²) than in the tetrahedral structures, we call these HDL-like structures.

There are fluctuations between the LDL-like and HDL-like structures. Although the timescale of these fluctuations slows down as we cool the liquid, the molecules in the asymmetric structures with distorted H-bonds fluctuate more and more frequently into tetrahedral structures with four strong H-bonds, which grow in size since the balance between enthalpy and entropy in the free energy shifts more and more to favor enthalpy with decreasing temperature. There is also a continuous change in the structure of the HDL-like species with temperature. The switching time of OH groups participating in strong or weak/broken H-bonding is furthermore expected to slow down and the amplitude in the motion to decrease with temperature. The HDL-like regions will approach more and more tetrahedral character with strong H-bonds as in high-density ices with many interstitials rather than as in hexagonal ice. Here we propose that as the HDL-like structures become more symmetrical, similar to HDA ice, the two OH groups in the water molecule encounter more similar environments. This would lead to increased vibrational lifetime interference due to both OH groups contributing in the core-excited electronic state, rather than only one. This would make the line shape of the high-energy $1b_1''$ peak more symmetrical, similar to the $1b_1'$ peak, and also narrower from the smaller thermal motion at lower temperature. As water is supercooled the correlation length increases³ indicating that the LDL-like regions become significantly larger. We would therefore assume that there would be different subclasses of tetrahedral molecules depending on the long-range ordering, where some are in the center of the region and others at the boundary. This could lead to

variations in the position of the $1b_1$ emission energy and lead to a substantial broadening of the low-energy $1b_1'$ peak, which would be fully consistent with the fitting shown in Fig. 7.

V. SUMMARY

Though all of the six hypotheses have different strengths and weaknesses, we regard the most likely explanation for the subtle changes in the lone-pair spectral region to be provided by the 6th hypothesis with minor contributions from the other mechanisms. If we assume a plausible line-shape temperature dependence, the ratio between $1b_1'$ and $1b_1''$ becomes closer to what we expect, where the now smaller deviation from the expected behavior could come from beam-induced local structural transformations of tetrahedral to distorted H-bonds. Clearly, this requires further investigation in the future utilizing both experiments and theory. Here, we would like to remark that the interpretation of XES of liquid water is indeed less straightforward than previously anticipated and other assumptions, such as temperature-dependent line shapes and potential beam-induced structural transformations of water, may be necessary to explain XE spectra of water upon deep supercooling. To further determine the line shape in the supercooled regime, it would be essential to measure water with superior energy resolution.

ACKNOWLEDGEMENTS

We acknowledge the National Science Foundation (US) (Grant No. CHE-0809324), Office Basic Energy Sciences (BES) through SSRL. We also acknowledge the Department of Energy through the SLAC Laboratory Directed Research and Development Program, Office of Basic Energy Sciences (BES) through SSRL and LCLS, the AMOS program within the Chemical Sciences, Geosciences, and Biosciences Division of the Office of Basic Energy Sciences, the Swedish Research Council, Lennanders Stiftelse, the Volkswagen Stiftung, and the Helmholtz Virtual Institute Dynamic Pathways in Multidimensional Landscapes for financial support. Portions of this research were carried out at LCLS at the SLAC National Accelerator Laboratory. LCLS is an Office of Science User Facility operated for DOE Office of Science by Stanford University. Support from LCLS staff is gratefully acknowledged. The SXR Instrument is funded by a consortium whose membership includes the LCLS, Stanford University through the Stanford Institute for Materials Energy Sciences (SIMES), Lawrence Berkeley National Laboratory (LBNL), University of Hamburg through the BMBF priority program FSP 301, and the Center for Free Electron Laser Science (CFEL). We thank Nils Mårtensson from Uppsala University and Franz Hennies from the MAX IV Laboratory for making available the XE spectrometer. The calculations were performed on resources provided by the Swedish National Infrastructure for Computing (SNIC) at the HPC2N center.

REFERENCES

1. Kanno, H. & Angell, C. A. Water: Anomalous compressibilities to 1.9 kbar and correlation with supercooling limits. *J. Chem. Phys.* **70**, 4008 (1979).
2. Speedy, R. J. & Angell, C. A. Isothermal compressibility of supercooled water and evidence for a thermodynamic singularity at -45°C . *J. Chem. Phys.* **65**, 851 (1976).
3. Huang, C. et al. Increasing correlation length in bulk supercooled H_2O , D_2O and NaCl solution determined from small angle x-ray scattering. *J. Chem. Phys.* **133**, 134504 (2010).
4. Mason, B. J. The supercooling and nucleation of water. *Advances in Physics* **7**, 221-234 (1958).
5. Poole, P. H., Sciortino, F., Essmann, U. & Stanley, H. E. Phase-Behavior of Metastable Water. *Nature* **360**, 324-328 (1992).
6. Sastry, S., Debenedetti, P. G., Sciortino, F. & Stanley, H. E. Singularity-free interpretation of the thermodynamics of supercooled water. *Phys. Rev. E* **53**, 6144-6154 (1996).
7. Angell, C. A. Insights into Phases of Liquid Water from Study of Its Unusual Glass-Forming Properties *Science* **319**, 582 (2008).
8. Limmer, D. T. & Chandler, D. The putative liquid-liquid transition is a liquid-solid transition in atomistic models of water. *J. Chem. Phys.* **135**, 134503 (2011).
9. Gallo, P. & Sciortino, F. Ising Universality Class for the Liquid-Liquid Critical Point of a One Component Fluid: A Finite-Size Scaling Test. *Phys. Rev. Lett.* **106**, 177801 (2012).
10. Kesselring, T. A., Franzese, G., Buldyrev, S. V., Herrmann, H. J. & Stanley, H. E. Nanoscale Dynamics of Phase Flipping in Water near its Hypothesized Liquid-Liquid Critical Point. *Scientific Reports* **2**, 474 (2012).
11. Kesselring, T. A., Lascaris, E., Franzese, G. & Stanley, H. E. Finite-size scaling investigation of the liquid-liquid critical point in ST2 water and its stability with respect to crystallization. *J. Chem. Phys.* **138**, 244506 (2013).
12. Limmer, D. T. & Chandler, D. The putative liquid-liquid transition is a liquid-solid transition in atomistic models of water. II. *J. Chem. Phys.* **138**, 214504 (2013).
13. Palmer, J. C., Car, R. & Debenedetti, P. G. The liquid-liquid transition in supercooled ST2 water: a comparison between umbrella sampling and well-tempered dynamics. *Faraday Discussion* **167** (2013).
14. Palmer, J. C. et al. Metastable liquid-liquid transition in a molecular model of water. *Nature*, 385-388 (2014).
15. Speedy, R. J. Stability-limit conjecture. An interpretation of the properties of water. *J. Phys. Chem.* **86**, 982 (1982).
16. Moore, E. B. & Molinero, V. Structural Transformation in Supercooled Water Controls the Crystallization Rate of Ice. *Nature* **479**, 506-508 (2011).
17. Sellberg, J. A. et al. Ultrafast X-ray probing of water structure below the homogeneous ice nucleation temperature. *Nature* **510**, 381-384 (2014).
18. Nilsson, A. & Pettersson, L. G. M. Perspective on the Structure of Liquid Water. *Chem. Phys.* **389**, 1-34 (2011).
19. Fuchs, O. et al. Isotope and temperature effects in liquid water probed by x-ray absorption and resonant x-ray emission spectroscopy. *Phys. Rev. Lett.* **100**, 027801 (2008).
20. Tokushima, T. et al. High Resolution X-ray Emission Spectroscopy of Liquid Water: The Observation of Two Structural Motifs. *Chem. Phys. Lett.* **460**, 387-400 (2008).
21. Lange, K. M. et al. High resolution X-ray emission spectroscopy of water and aqueous ions using the micro-jet technique. *Chem. Phys.* **377**, 1-5 (2010).
22. Lange, K. M. et al. On the origin of the hydrogen-bond-network nature of water: X-ray absorption and emission spectra of water-acetonitrile mixtures. *Angew. Chem.* **123**, 1-6 (2011).
23. Lange, K. M. et al. X-ray emission from pure and dilute H_2O and D_2O in a liquid microjet: Hydrogen bonds and nuclear dynamics. *Phys. Rev. B* **85**, 155104 (2012).
24. Nilsson, A., Huang, C. & Pettersson, L. G. M. Fluctuations in Ambient Water. *J. Mol. Liq.* **176**, 2-16 (2012).
25. Nilsson, A. et al. Resonant Inelastic X-Ray Scattering of Liquid Water. *J. El. Struc. Rel. Phenom.* **188**, 84-100 (2013).
26. Tokushima, T. et al. High resolution X-ray emission spectroscopy of water and its assignment based on two structural motifs. *J. El. Spec. Rel. Phen.* **177**, 192-205 (2010).
27. Tokushima, T. et al. Polarization dependent resonant x-ray emission spectroscopy of D_2O and H_2O water; assignment of the local molecular orbital symmetry. *J. Chem. Phys.* **136**, 044517 (2012).

28. Huang, C. et al. The Inhomogeneous Structure of Water at Ambient Conditions. *Proc. Natl. Acad. Sci. (USA)* **106**, 15214–15218 (2009).
29. Pettersson, L. G. M. & Nilsson, A. The structure of water; from ambient to deeply supercooled. *Journal of Non-Crystalline Solids* **407**, 399-417 (2015).
30. Fuchs, O. et al. Reply to Comment on “Isotope and Temperature Effects in Liquid Water Probed by X-Ray Absorption and Resonant X-Ray Emission Spectroscopy”. *Phys. Rev. Lett.* **100**, 249802 (2008).
31. Odellius, M. Information Content in O[1s] K-edge X-ray Emission Spectroscopy of Liquid Water. *J. Phys. Chem. A* **113**, 8176-8181 (2009).
32. Odellius, M. Molecular dynamics simulations of fine structure in oxygen K-edge x-ray emission spectra of liquid water and ice. *Phys. Rev. B* **79**, 144204 (2009).
33. Forsberg, J. et al. Angular anisotropy of resonant inelastic soft x-ray scattering from liquid water. *Phys. Rev. B* **79**, 132203 (2009).
34. Ljungberg, M. P., Nilsson, A. & Pettersson, L. G. M. Semi-classical description of nuclear dynamics in x-ray emission of water. *Phys. Rev. B* **82**, 245115 (2010).
35. Ljungberg, M. P., Pettersson, L. G. M. & Nilsson, A. Vibrational interference effects in x-ray emission of a model water dimer: implications for the interpretation of the liquid spectrum *J. Chem. Phys.* **134**, 044513 (2011).
36. Schlotter, W. F. et al. The soft x-ray instrument for materials studies at the linac coherent light source x-ray free-electron laser. *Review of Scientific Instruments* **83**, 043107 (2012).
37. Schreck, S. et al. Reabsorption of Soft X-ray Emission at High X-ray Free-Electron Laser Fluences. *Phys. Rev. Lett.* **113**, 153002 (2014).
38. Nordgren, J. et al. x-ray spectrometer. *Rev. Sci. Instrum.* **60**, 1690 (1989).
39. Kunnus, K. et al. A setup for resonant inelastic soft x-ray scattering on liquids at free electron laser light sources. *Review of Scientific Instruments* **83**, 123109 (2012).
40. DePonte, D. P. et al. Gas dynamic virtual nozzle for generation of microscopic droplet streams. *J. Phys. D: Appl. Phys.* **41**, 195505 (2008).
41. Rayleigh, F. R. S. On the Instability of Jets. *Proc. London Math. Soc.* **10**, 4-12 (1879).
42. Knudsen, M. Die maximale Verdampfungsgeschwindigkeit des Quecksilbers. *Ann. Phys.* **352**, 697-708 (1915).
43. Maa, J. R. Evaporation Coefficient of Liquids. *Industrial & Engineering Chemistry Fundamentals* **6**, 504-518 (1967).
44. Smith, J. D., Cappa, C. D., Drisdell, W. S., Cohen, R. C. & Saykally, R. J. Raman Thermometry Measurements of Free Evaporation from Liquid Water Droplets. *J. Am. Chem. Soc.* **128**, 12892-12898 (2006).
45. Tokushima, T., Harada, Y., Ohashi, H., Senba, Y. & Shin, S. High performance slit-less spectrometer for soft x-ray emission spectroscopy. *Review of Scientific Instruments* **77**, 063107 (2006).
46. Harada, Y. et al. Ultrahigh resolution soft x-ray emission spectrometer at BL07LSU in SPring-8. *Review of Scientific Instruments* **83**, 013116 (2012).
47. Strocov, V. N., Schmitt, T., Flechsig, U., Patthey, L. & Chiuzbăian, G. S. Numerical optimization of spherical variable-line-spacing grating X-ray spectrometers. *Journal of Synchrotron Radiation* **18**, 134-142 (2011).
48. Ogawa, M. et al. Development of soft x-ray time-resolved photoemission spectroscopy system with a two-dimensional angle-resolved time-of-flight analyzer at SPring-8 BL07LSU. *Review of Scientific Instruments* **83**, 023109 (2012).
49. Møgelhøj, A. et al. Ab initio van der Waals interactions in simulations of water alter structure from mainly tetrahedral to high-density-like. *J. Phys. Chem. B* **115** 14149–14160 (2011).
50. Föhlisch, A. et al. Ground state interpretation of XES of adsorbates. *Phys. Rev. B* **16**, 16229 (2000).
51. Köster, A. M. et al. (deMon developers, Mexico-City, 2011).
52. Hammer, B., Hansen, L. B. & Nørskov, J. K. Exchange functional rPBE. *Phys. Rev. B* **59**, 7413 (1999).
53. Kutzelnigg, W., Fleischer, U. & Schindler, M. *NMR-Basic Principles and Progress* (Springer Verlag, Heidelberg, 1990).
54. Igel-Mann, G., Stoll, H. & Preuss, H. Pseudopotentials for main group elements (IIIa through VIIa). *Molecular Physics* **65**, 1321-1328 (1988).
55. Gilberg, E., Hanus, M. J. & Foltz, B. Investigation of the Electronic-Structure of Ice by High-Resolution X-Ray Spectroscopy. *J. Chem. Phys.* **76**, 5093-5097 (1982).
56. Wikfeldt, K. T., Nilsson, A. & Pettersson, L. G. M. Spatially Inhomogeneous Bimodal Inherent Structure in Simulated Liquid Water. *Phys. Chem. Chem. Phys.* **13** 19918-19924 (2011).
57. Nordlund, D. et al. The Electronic Structure of Liquid Water Studied Using Photoelectron Spectroscopy. *Chem. Phys. Lett.* **460**, 86 (2008).

58. Winter, B. et al. Full valence band photoemission from liquid water using EUV synchrotron radiation. *J. Phys. Chem. A* **108**, 2625 (2004).
59. Nishizawa, K., Kurahashi, N., Sekiguchi, K. & Mizuno, T. High-resolution soft X-ray photoelectron spectroscopy of liquid water *Phys. Chem. Chem. Phys.* **13**, 413-417 (2011).
60. Winter, B., Aziz, E. F., Hergenahn, U., Faubel, M. & Hertel, I. V. Hydrogen bonds in liquid water studied by photoelectron spectroscopy. *J. Chem. Phys.* **126**, 124504 (2007).
61. Nilsson, A. et al. The hydrogen bond in ice probed by soft x-ray spectroscopy and density functional theory. *J. Chem. Phys.* **122**, 154505 (2005).
62. Thürmer, S. et al. On the nature and origin of dicationic, charge-separated species formed in liquid water on X-ray irradiation. *Nat. Chem.* **5**, 590-596 (2013).
63. Sellberg, J. A. et al. Comparison of x-ray absorption spectra between water and ice: New ice data with low pre-edge absorption cross-section. *The Journal of Chemical Physics* **141**, 034507 (2014).
64. Mishima, O., Calvert, L. D. & Whalley, E. 'Melting ice' I at 77 K and 10 kbar: a new method of making amorphous solids. *Nature* **310**, 393-395 (1984).
65. Nibbering, E. T. J. & Elsaesser, T. Ultrafast vibrational dynamics of hydrogen bonds in the condensed phase. *Chem. Rev.* **104**, 1887-1914 (2004).
66. Wikfeldt, K. T., Huang, C., Nilsson, A. & Pettersson, L. G. M. Enhanced small-angle scattering connected to the Widom line in simulations of supercooled water. *J. Chem. Phys.* **134**, 214506 (2011).
67. Bertie, J. E. & Lan, Z. Infrared Intensities of Liquids XX: The Intensity of the OH Stretching Band of Liquid Water Revisited, and the Best Current Values of the Optical Constants of H₂O(l) at 25°C between 15,000 and 1 cm⁻¹. *Applied Spectroscopy* **50**, 1047-1057 (1996).
68. Fecko, C. J., Eaves, J. D., Loparo, J. J., Tokmakoff, A. & Geissler, P. L. Ultrafast hydrogen-bond dynamics in the infrared spectroscopy of water. *Science* **301**, 1698-1702 (2003).
69. Soper, A. K. & Ricci, M. A. Structures of high-density and low-density water. *Phys. Rev. Lett.* **84**, 2881-2884 (2000).
70. Nilsson, A. et al. X-ray Absorption Spectroscopy and X-ray Raman Scattering of Water; An Experimental View. *J. El. Spec. Rel. Phen.* **177**, 99-129 (2010).
71. Lishchuk, S. V., Malomuzh, N. P. & Makhlaichuk, P. V. Why thermodynamic properties of normal and heavy water are similar to those of argon-like liquids? . *Phys. Lett. A* **374**, 2084 (2010).
72. Skinner, L. B. et al. Benchmark oxygen-oxygen pair-distribution function of ambient water from x-ray diffraction measurements with a wide Q-range. *J. Chem. Phys.* **138**, 074506 (2013).

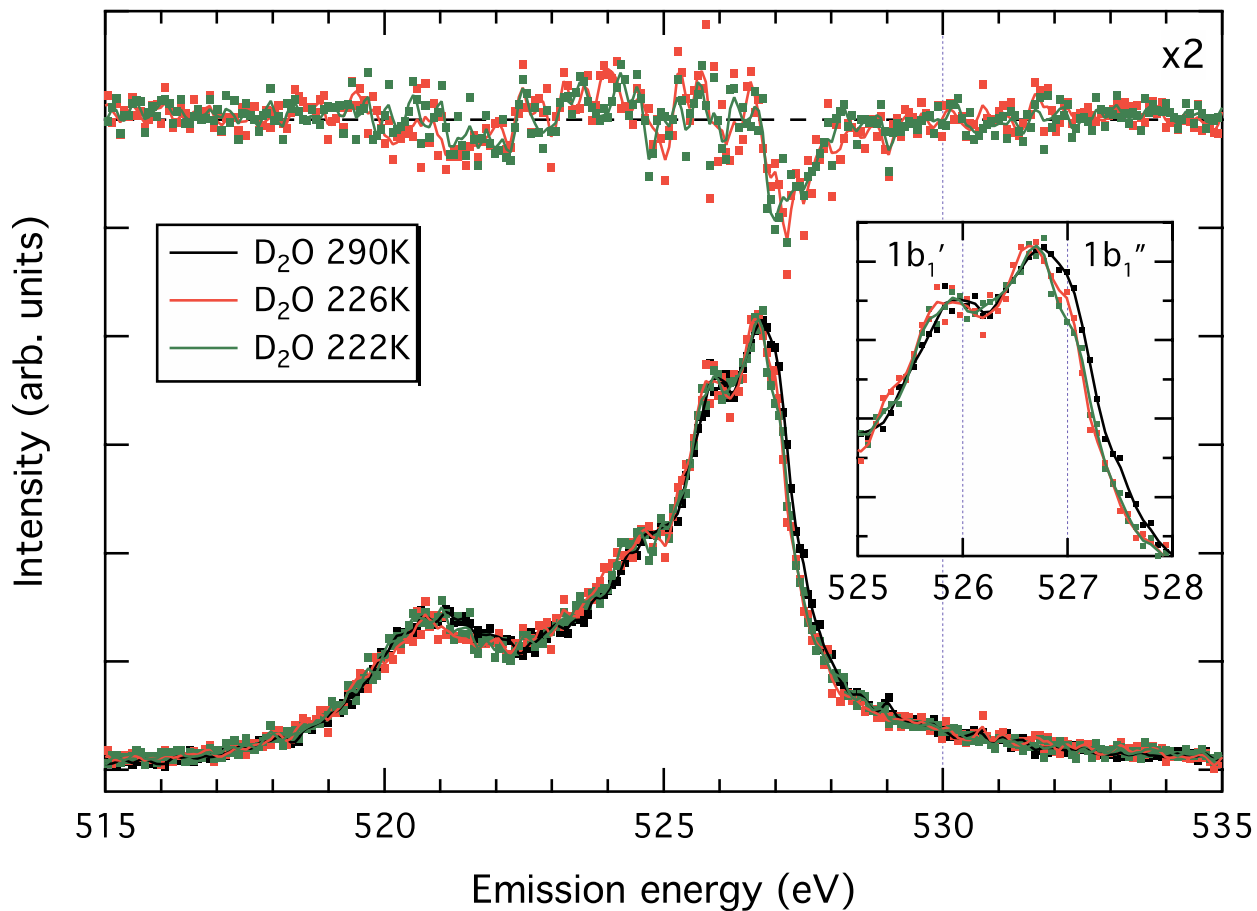


FIG. 1. O K-edge XE spectra of liquid D₂O measured at ~290 K (black curve), 226 K (red curve), and 222 K (green curve). The XE spectra were recorded at LCLS using an incident photon energy of 550 eV, a nominal pulse length of 100 fs, and a beam focus of $75 \times 520 \mu\text{m}^2$ (horizontal \times vertical) at the interaction point, corresponding to a peak fluence of 0.27 J/cm^2 . The top shows the difference spectra (magnified by a factor of 2) with respect to the XE spectrum of D₂O at 290 K. The inset shows an enlarged view of the lone-pair ($1b_1$) region of the XE spectra. All XE spectra were background subtracted with an 8th order polynomial and area normalized between 500 and 550 eV.

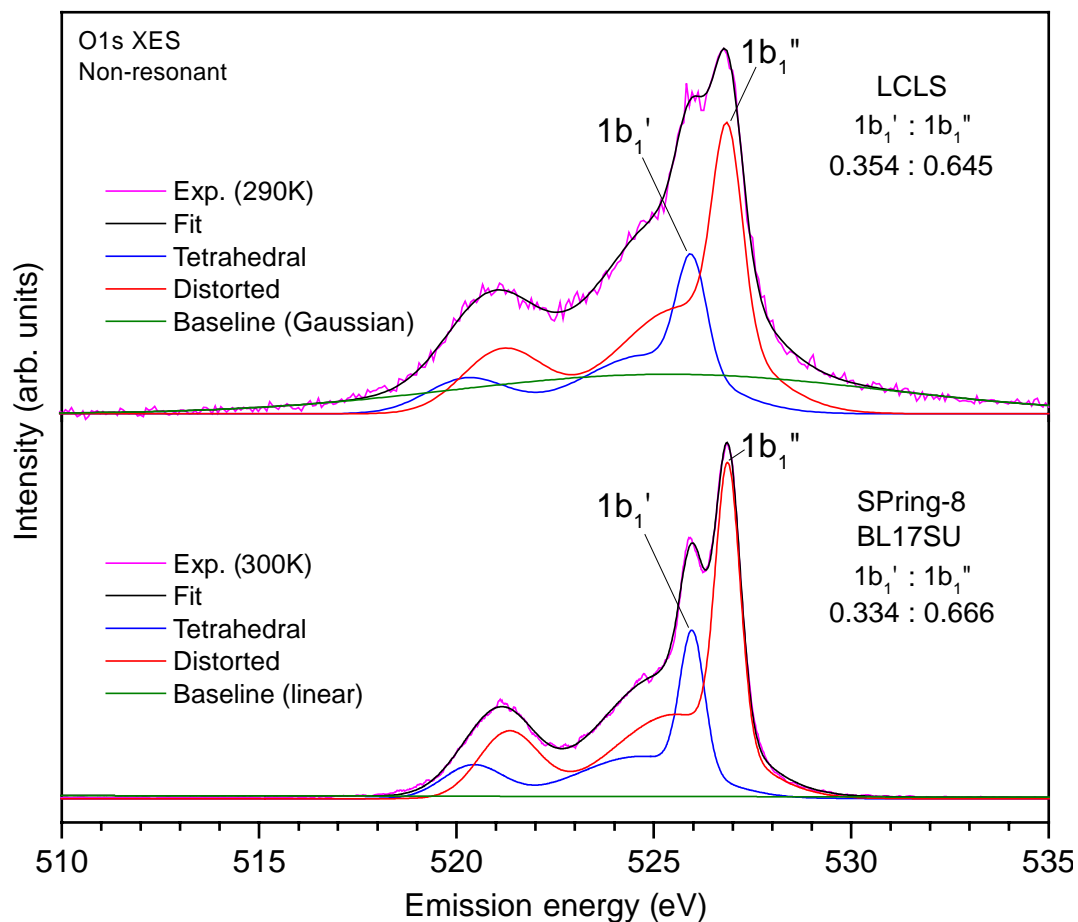


FIG. 2. Gaussian peak-fit analysis of O K-edge XE spectra of liquid D_2O measured at LCLS at ~ 290 K (top) and SPring8 at 300 K (bottom). The spectra are decomposed into two sets of three Gaussians, corresponding to the molecular orbitals $1b_2$, $3a_1$, and $1b_1$. Each set represents a molecular species and is separated by an absolute energy shift, representing a core-level shift between the two hypothesized species, and an amplitude difference, representing the relative population of each species. The high-energy set (red curve) corresponds to species with distorted H-bonds, whereas the low-energy set (blue curve) corresponds to tetrahedrally H-bonded species. For the LCLS data, a Gaussian background (green curve) is necessary to describe the diffuse background scattering from the grating due to imperfections most likely originating from contamination.

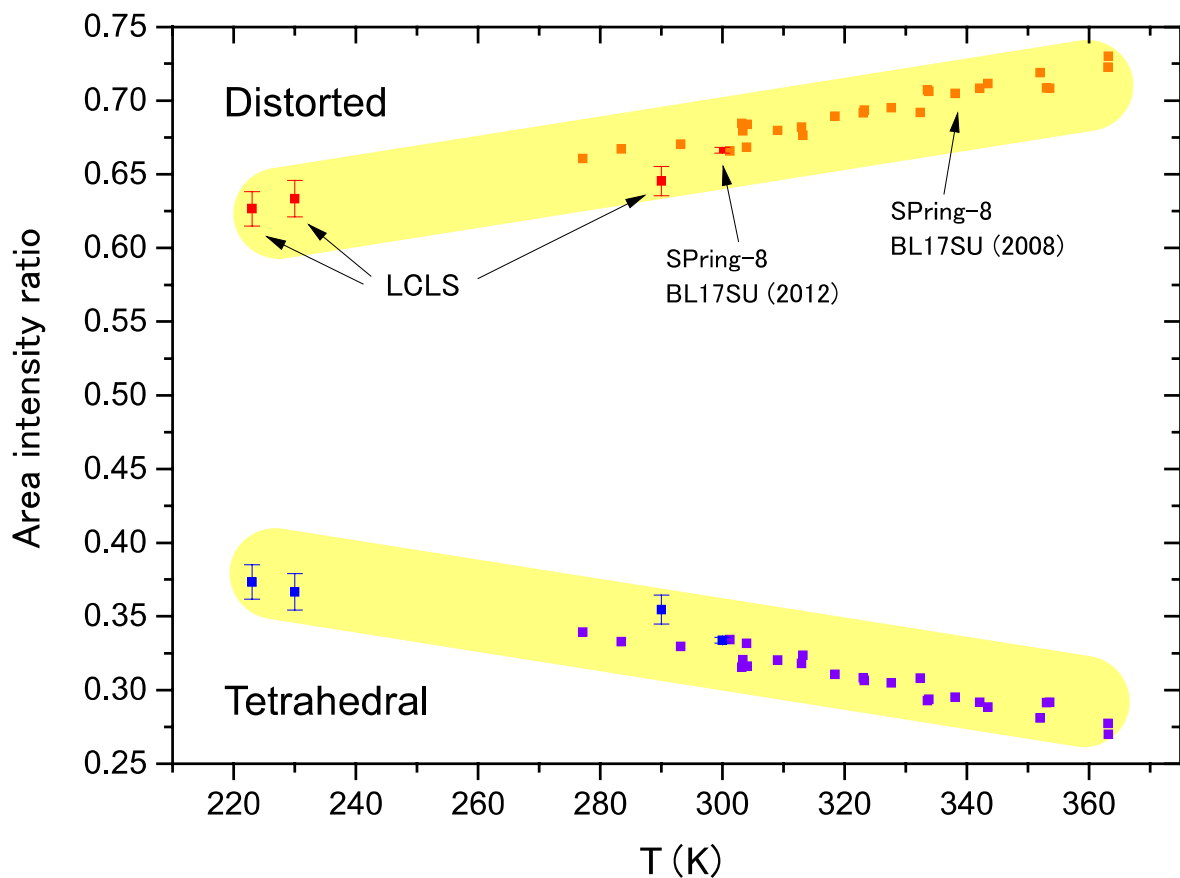


FIG. 3. Population analysis of tetrahedrally H-bonded species (blue and purple markers) and species with distorted H-bonds (red and orange markers) deduced from Gaussian peak-fit analysis of O K-edge XE spectra of liquid D_2O measured at LCLS in 2012, SPring-8 in 2012, and SPring-8 in 2008²⁸ as marked in the figure. The vertical error bars for spectra measured at LCLS in 2012 and at SPring-8 in 2012 are estimated by the standard errors for the intensity area of each species, corresponding to one standard deviation in the confidence interval for the amplitude difference in the peak-fit analysis (Fig. 2). Within the model assumed, the tetrahedral species is a minority at all temperatures, which is in disagreement with recent x-ray scattering measurements¹⁷.

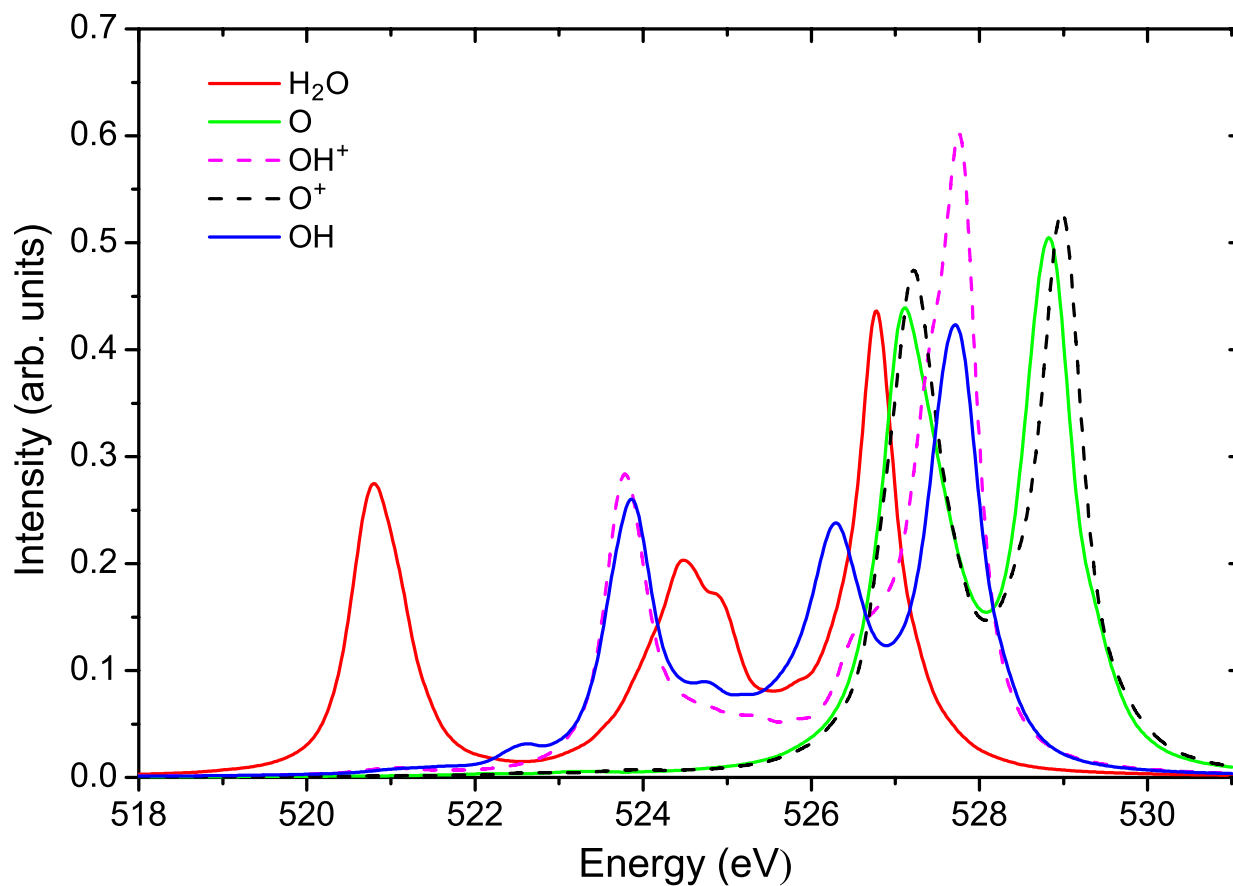


FIG 4. Computed XE spectra for H₂O (red solid curve) and neutral (solid curves) and positive (dashed curves) fragments of OH and atomic O in a sampling of 32 molecules water clusters (Methods). The same shift has been applied to all spectra such that the 1b₁ peak position of H₂O coincides with the experimental 1b₁'' peak position. Contributions from the fragments appear in the vicinity of the high-energy 1b₁'' peak but do not contribute to the 1b₁' peak at lower emission energy.

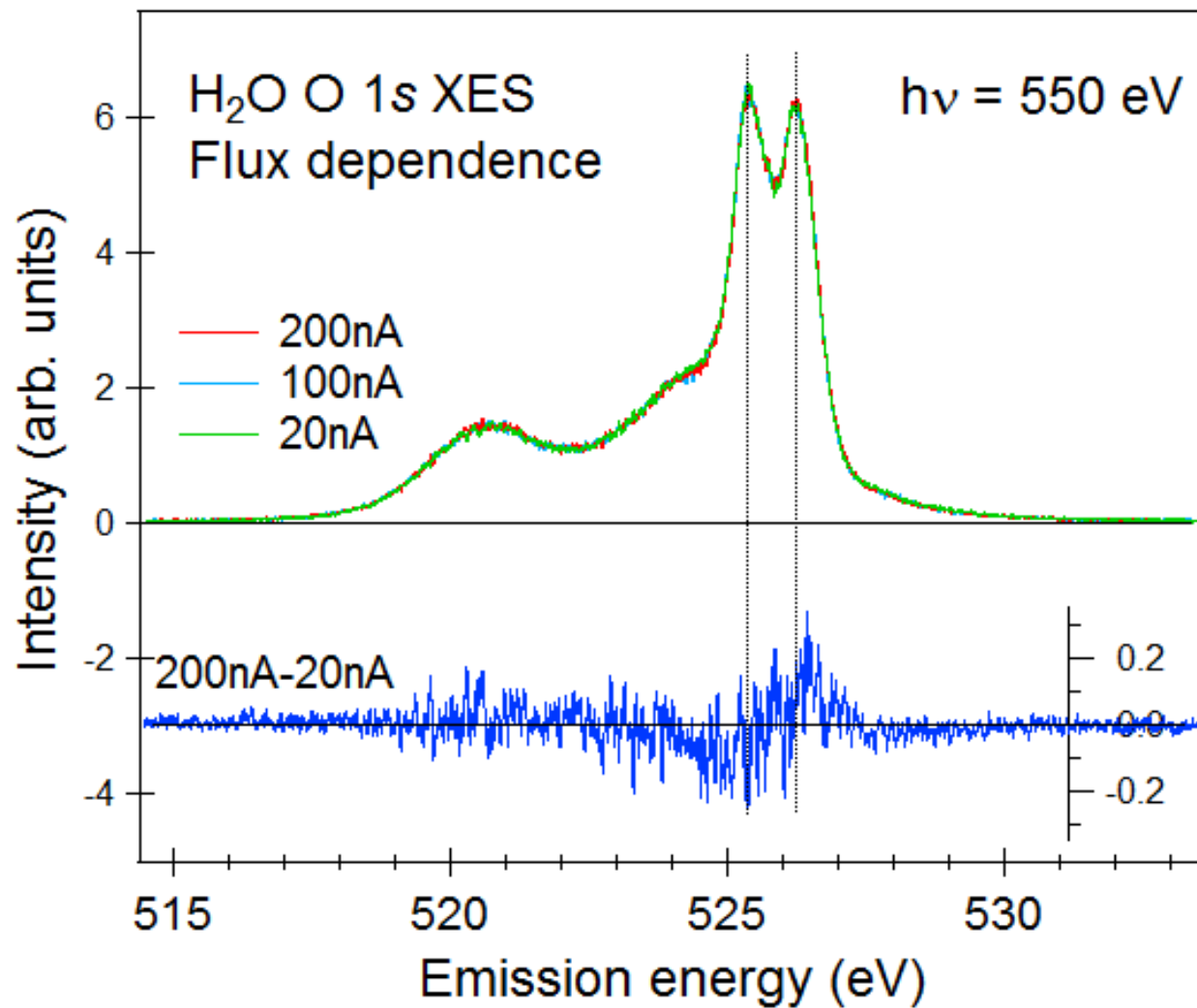


FIG. 5. Flux-dependent O K-edge XE spectra of liquid H₂O measured at BL07LSU at SPring-8. Incident beam intensity was measured by a drain current of the post-focusing mirror placed 150 mm upstream of the sample position, and tuned from minimum (20 nA, green curve) to maximum (200 nA, red curve). The intensity was normalized by the displayed area intensity. The lower blue curve is the difference spectrum between the normalized 200 nA and 20 nA spectra.

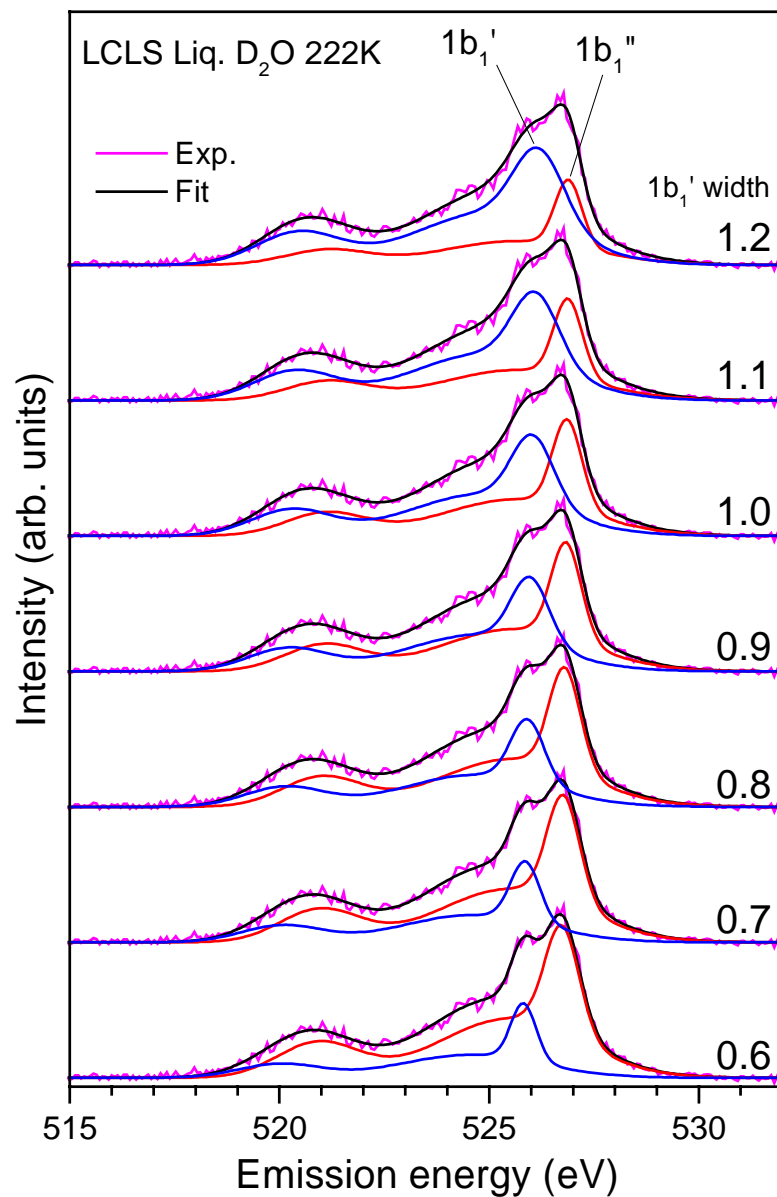


FIG. 6. Peak-fit analysis of the XE spectrum of liquid D_2O at 222 K measured at LCLS as a function of different line width of the $1b_1'$ (given to the right of each spectrum) and $1b_1''$ components. The $1b_1'/1b_1''$ intensity ratio as well as the $1b_1'/1b_1''$ line width ratio increases monotonically with increasing $1b_1'$ line width.

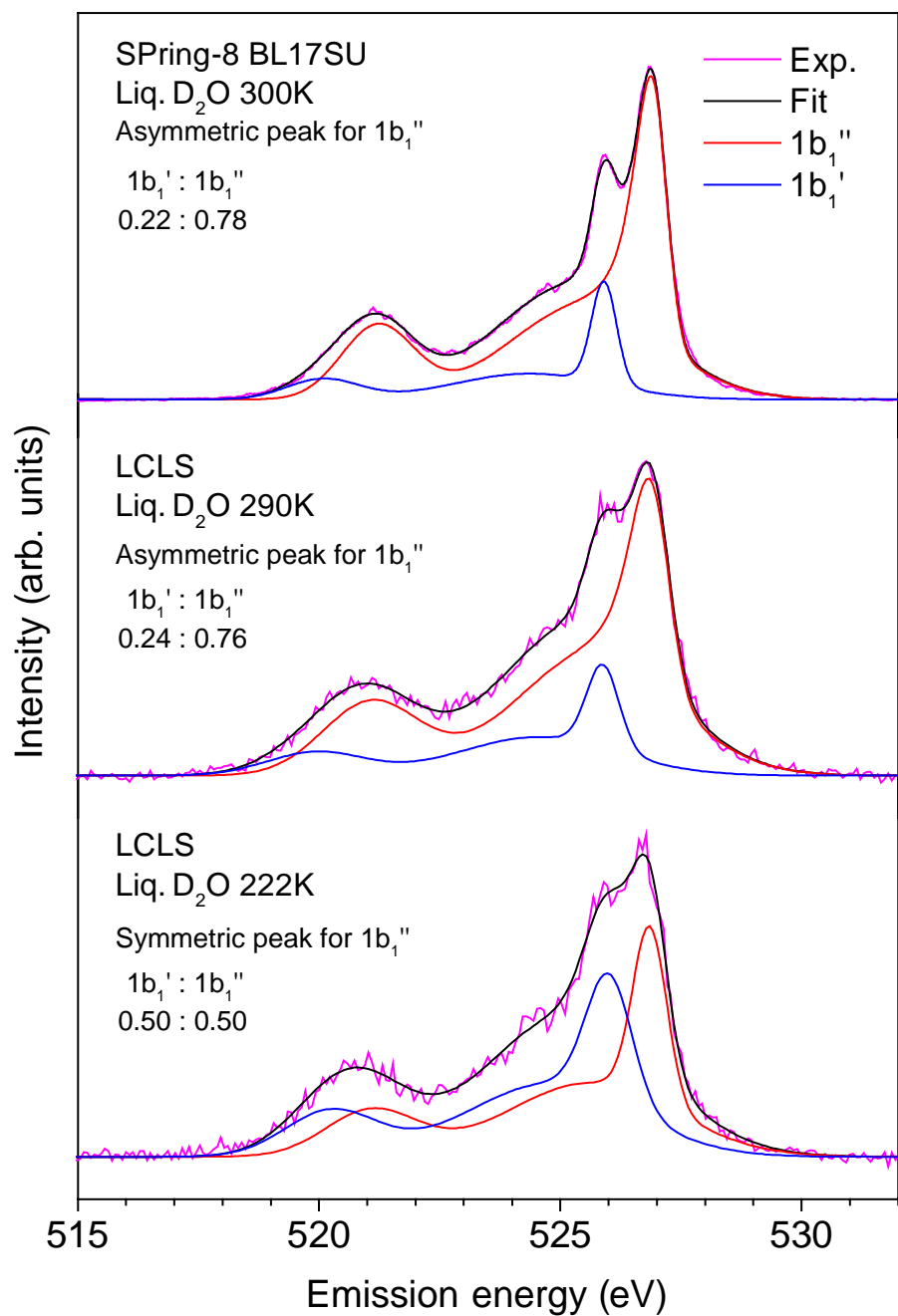


FIG. 7. Line-width dependent peak-fit analysis of XE spectra from SPring-8 at 300 K (top) and LCLS at ~290 K (middle) with a dominating high-energy 1b₁'' component and from LCLS at 222 K (bottom) with a close to 1:1 ratio between the 1b₁' and 1b₁'' components. The spectrum at 222 K has a broader 1b₁' peak and a symmetric 1b₁'' peak compared to the spectra close at higher temperature with narrower 1b₁' peaks and asymmetric 1b₁'' peaks.